UNIL | Université de Lausanne
Faculté de biologie
et de médecine

LREN
Laboratoire de Recherche en Neuro-Imagerie

Mémoire de Maîtrise en médecine No 2070

Creation of new tissue priors for automated delineation of basal ganglia in magnetic resonance imaging

Student
Samuel Frésard

Tutor
Prof. Bogdan Draganski
Laboratoire de Recherche en Neuroimagerie, CHUV

Co-tutor
Sara Lorio
Laboratoire de Recherche en Neuroimagerie, CHUV

Expert
Dr. Christian Wider, PD
Service de Neurologie, CHUV

Lausanne, March 2016

Table of Contents

Abstract

The advent of magnetic resonance (MR) imaging has brought to the field of neurosciences the stupendous ability of *in-vivo* study of the human brain's tissular properties. More recent developments in the field of computational anatomy have led to automated approaches of volumetric assessment of the brain in voxel-based morphometry (VBM). VBM has provided significant understanding about physiopathology of brain diseases, including psychiatric and neurodegenerative diseases (NDDs). VBM performs tissue classification using algorithms that rely on contrast between tissues and probabilistic maps, termed tissue priors. These algorithms have provided accurate and satisfying study of the human cortex. However, tissue classification of deep gray matter such as the basal ganglia has been found to be largely unreliable. Conventional T1-weighted MR imaging provides lower contrast for deep gray matter than the cortical gray matter. The main reason for this contrast bias is the higher iron concentration in those structures. Moreover, iron deposits increase in the normal ageing adult and reach pathological concentrations in a wide number of neurological disorders including NDDs. Accurate assessment is thus challenged for subcortical structures in both health and disease.

Recently, quantitative MR imaging (qMRI) has been developed to allow quantitative assessment of tissular microstructure of the brain. Those new sequences, such as magnetization transfer saturation (MT) and effective transverse relaxation rate (R2*) parameter maps, provide better contrast by displaying quantitative surrogates for myelin and iron respectively. MT parameter maps have shown to overcome high iron content sensitivity and to be highly suitable for automated delineation of the basal ganglia. Although MT parameter maps provide sufficient contrast, current tissue priors remain insufficient to provide satisfying tissue classification. In this work, we created robust and accurate tissue priors for deep gray matter.

Key words : basal ganglia – tissue priors – iron – qMRI – VBM

Introduction

Background

Basal ganglia : anatomy, function and associated diseases

Anatomy of basal ganglia

The human central nervous system (CNS) is composed of the brain and the spinal cord. The CNS is divided in two major tissue types : the gray matter (GM) and the white matter (WM). The main difference is that GM is formed of cell bodies of neurons and axonal projections of neurons as of WM only contains axons without neuronal cell bodies. Brain GM is either located at the surface of the brain as an outer layer over the brain WM and is called the cortex, or arranged in nuclei within the WM and is called the deep gray matter.
Deep gray matter pertaining to the telencephalon is termed the basal ganglia. Namely, the basal ganglia are composed of the caudate nucleus (CN), the putamen and the globus pallidus (GP) that is subdivided into external and internal segments (figure 1). The putamen and the CN form the same functional unit called the striatum. The putamen and the GP are morphologically closely related and form together the lenticular nucleus. The diencephalic deep gray matter is mainly composed of the thalamus. The mesencephalon (upper division of brain stem) contains deep gray matter that is closely connected to the previously described structures : the subthalamic nucleus (STN), the substantia nigra (SN) and the red nucleus (RN ; not illustrated, behind SN) (figure 1).

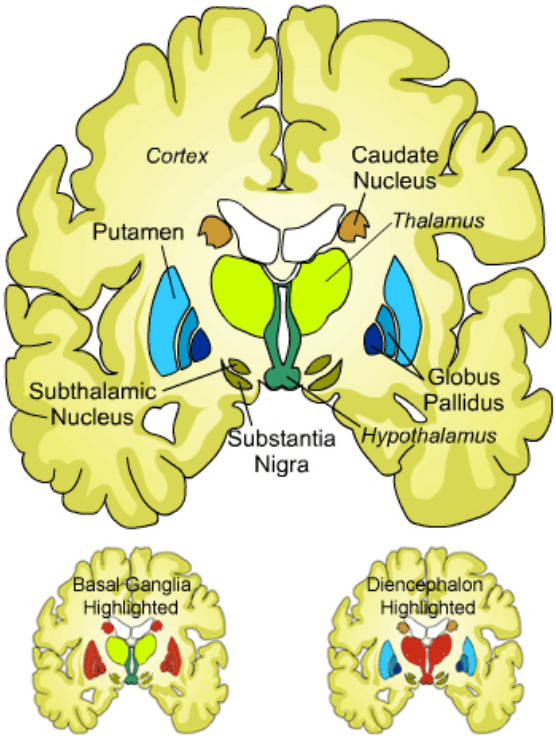

Figure 1 : Illustration of deep gray matter structures : the basal ganglia (telencephalon), the thalamus (diencephalon), STN and SN (mesencephalon).
Adapted illustration used with permission of Huntington's Disease Outreach Project for Education at Stanford (HOPES), http://hopes.stanford.edu

Function of basal ganglia

The basal ganglia and their projections involve three primary functions : motor control, cognition and motivation (reward system).
Basal ganglia stock and mobilize complex learned motor tasks, such as writing, and provide motor initiation, integration and adjustment to the motor cortex to produce appropriate motor output to the muscles. Subcortical motor processing permits precise, fast and adapted movements.
The two latter functions – cognition and motivation – are essential to higher behavioral functioning. The high connectivity between the basal ganglia and with the other subcortical structures as well as with the cortex makes those nuclei the key structures for appropriate goal-directed and adaptive behaviors, habit formation and long-term planning. These require a high and complex integration of emotions, memory, cognitive planning and motivation with adaptive learning faculty to respond to internal and environmental cues. Therefore the basal ganglia play a crucial role for adapted motor and behavioral controls thus elaboration and execution of action plans (for review, see *Haber, 2014*) (1–3).

Diseases involving the basal ganglia

The diseases implying the basal ganglia exhibit a spectrum of disorders of various motor and neuropsychiatric features. Conditions such as essential tremor (ET) and dystonia are primarily motor disorders that arise from dysfunction of the basal ganglia. Conversely, other disorders involve principally neuropsychiatric characteristics as addiction, schizophrenia, borderline personality disorder and depression. However a lot of diseases implying the basal ganglia incorporate both dimensions in various degrees : Huntington disease (HD), Tourette syndrome, Parkinson disease (PD) and atypical parkinsonian syndromes (PSs), obsessive-compulsive disorder (OCD), stuttering, restless-legs syndrome and narcolepsy (3–5).
Overall these disorders affect a significant part of the population and account for high burden of disease. *In vivo* study of basal ganglia through magnetic resonance (MR) imaging has brought significant understanding of physiopathology and led to therapeutic methods such as deep brain stimulation (DBS), a neurosurgical procedure that implants an electrical stimulator on a specific brain target. DBS has shown to be an effective treatment method for PD, ET, dystonia, refractory and severe depression and OCD with possible expansion to other basal ganglia-related diseases (6–8).
Therefore further study of function in health and disease along with improvement of subcortical gray matter imaging is essential to improve and create new innovative diagnostic and treatment methods.

Commonly used tissue classification methods in magnetic resonance imaging

MR imaging allowed considerable progress in the field of neuroscience and enabled the *in-vivo* study of the human brain in both health and disease.
Voxel-based morphometry (VBM) has been the first technique to provide quantitative morphometric assessment of brain structure from MR images. Regions of interest (ROI) were initially delineated manually or semi-manually to compute the volume of a particular structure. Laborious work of manual delineation and limitation of study to selected ROI led to new automated approaches (9).
VBM classifies brain images into different tissue classes : GM, WM and cerebrospinal fluid (CSF). This process relies, firstly, on voxel (*volume element*, three-dimensional pixel) intensity and secondly on Bayesian probabilistic analysis of voxel location. A procedure termed image

registration is applied to an individual brain to compare population of subjects. An image is registered into a normalized stereotaxic template. The Montreal Neurological Institute (MNI) atlas is the most commonly used stereotaxic space in brain normalization.
Probabilistic tissue classification uses a tissue probability map (TPM) on normalized individual data. A TPM is a bundle of pre-established maps in normalized space, called tissue priors that individually indicate spatial probability to pertain to a certain tissue class. A TPM has classically tissue priors for 4 tissue classes : GM, WM, CSF and "other" (figure 2). Tissue priors express tissue-belonging probability for every voxel based on gray-intensity scale so that sum of tissue priors is 1 (white) in every voxel. Appropriate tissue priors are generated from healthy population with comparable representation of genders and wide age span in adults, and are based on the best to-date tissue segmentation model.
A TPM is applied to the registered data of an individual brain using a classification algorithm, such as statistical parametric mapping (SPM) (Wellcome Trust Centre for Neuroimaging, London, UK ; http://www.fil.ion.ucl.ac.uk/spm). Application of TPM on the subject's normalized data gives posterior tissue probability at each location of the subject's brain image. The image is then un-normalized into native space. Subsequent volumetric study of each tissue class can be applied (for review, consult *Ashburner and Friston, 2005)* (10).

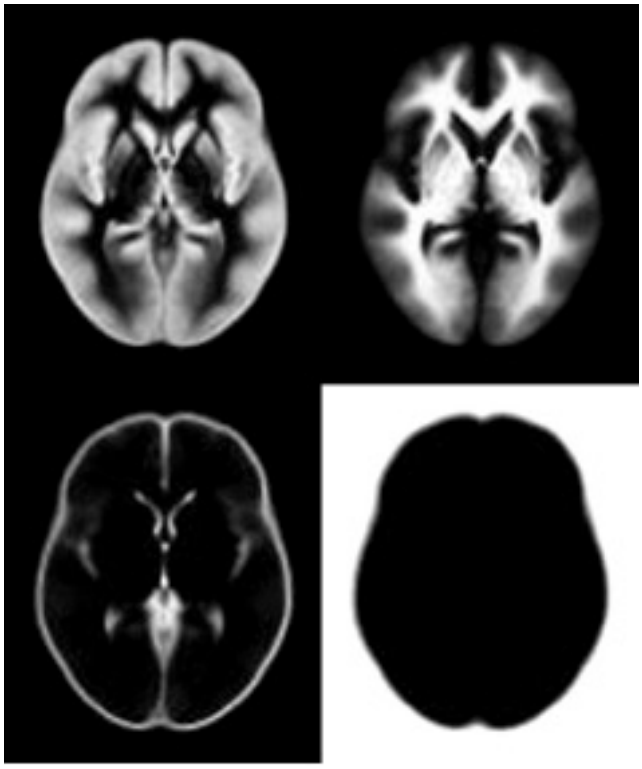

Figure 2 : Tissue probability map for GM, WM, CSF and "other" (10)**.**

Basal ganglia's morphological assessment limitations in computational anatomy

Low reliability of common VBM techniques of subcortical structures

Although MRI-derived morphometry of cortical gray matter is highly reliable, visualization and tissue classification of subcortical structures remain challenging due to poor tissue contrast and lack of accurate priors in tissue classification.
In T1-based imaging, deep gray matter provides lower intensity than cortical gray matter by both intrinsic tissue signal properties as well as the contrast with surrounding tissue types

lowering contrast-to-noise ratio (CNR ; contrast quality between GM and WM). Reliability of tissue classification measures varies greatly by structure. GP, RN, SN and STN appear to be the least reliable subcortical structures for segmentation. The difference of intrinsic tissue signal quality between cortical and subcortical gray matter relies, firstly, on high iron content of deep gray matter that interferes with relaxation time during signal acquisition. Secondly, the nature of the microstructure of nuclei is composed of intertwined axonal tracts and neuronal bodies – rather than layered structure in cortex – and is below the resolution limits of standard T1w imaging (~1 mm) thus further reducing contrast by partial volume averaging (11–13). Problems regarding tissue priors are explored in details further.

Brain metallic ions and magnetic susceptibility

The main reason of poor quality imaging of deep gray matter in VBM is presence of higher iron tissue concentration.

The most common metallic ions essential to brain function such as sodium, potassium, calcium, magnesium are paramagnetic or diamagnetic for zinc and have no impact on MR images because of their low magnetic susceptibility (degree of magnetization of a material in response of an applied magnetic field and, thereby, the ability to distort the applied magnetic field). However ions of the transition group such as iron, manganese, and copper exhibit significant magnetic moments and have the potential of affecting MR contrast. Manganese and copper are paramagnetic but have high magnetic susceptibility, however nonpathological concentrations of copper and manganese are too low to produce detectable MR contrast bias. Iron is ferromagnetic and have consequently extremely high magnetic susceptibility that is capable to produce significant distortions of the magnetic field in physiological concentrations (14–16).

Brain iron

There are two categories of iron forms in the brain : heme iron (iron contained in a hemic molecule found mainly hemoglobin but also enzymes as peroxidases) and nonheme iron consisting chiefly of iron-storing proteins such as ferritin and hemosiderin, iron-transporting proteins such as transferrin and ionic iron (ferrous iron, Fe^{2+} and ferric iron, Fe^{3+}). Both heme and nonheme iron plays an important role in physiology as an essential cofactor for a number of cellular processes such as gene expression, neuronal development, enzymatic reactions, dopamine, iron-sulfur cluster synthesis, and electron transport to provide usable chemical potential energy in the form adenosine triphosphate (ATP) in cellular respiration. This process is crucial to survival and function to any cell in aerobic organisms but is remarkably important in neurons due to their extreme metabolic activity (17).

Iron content in healthy and pathologic brain drew significant attention from researchers in the previous century. Numerous studies in the field of neurobiology and neurohistopathology provided detailed accounts on various iron molecular forms, topographic iron accumulation in both healthy and diseased brains.

In a nutshell, biochemical studies indicates that overall iron content is similar in WM and cortical GM (18). Postmortem studies demonstrated that relative to the basal ganglia there is much less stainable iron in the cerebral hemispheric white matter and cortex (19). Several biochemical assays revealed the highest iron concentration in GP, RN, SN and putamen regions (for review, see *Haacke et al, 2005*) (20). Ferritin distribution closely matches ionic iron distribution with similar levels in WM and cortical GM, and with concentrations in the basal ganglia two to three times greater than in the cerebral cortex. Transferrin appears to

be more evenly distributed in GM, compared to ferritin and ionic iron, with similar levels in the cortex and basal ganglia. However, transferrin concentrations are typically between 10 and 50 times lower than ferritin concentrations and binds only 2 molecules of iron compared to thousands for ferritin (18,20). On a cellular level, oligodendrocytes (myelin-building cells) account for the majority of iron deposit throughout the brain in the form of ionic iron, ferritin and transferrin. Basal ganglia appeared to have more iron-rich oligodendrocytes and ferritin-positive astrocytes (20,21).
In the healthy brain, iron concentration is age-dependent and shows significant increase after the age of 40 years old, particularly for putamen, CN, and GP and pulvinar (22).
Furthermore, pathologically high iron concentration in brain is observed in many neurodegenerative diseases (NDDs) : PD and PSs, Alzheimer disease (AD), HD, Friedreich ataxia and amyotrophic lateral sclerosis. The basal ganglia are the primary sites of iron deposits in most NDDs : substantia nigra pars compacta (SNpc) and GP in PD ; GP, putamen and CN in AD ; putamen, CN, and GP in HD. Brain iron is also known to increase in the basal ganglia under ischemic conditions (17,20).

Iron in magnetic resonance imaging

Ferritin and hemosiderin are considered to be the only forms of nonheme iron present in sufficient quantities to affect MR contrast in the human brain.
All magnetic materials present in tissues reduce both T1 and T2 relaxation times. Shorter T1 relaxation time will appear brighter while short T2 appear darker. The major effect of brain iron, by ferritin and hemosiderin, on MR images is a reduction in T2 with smaller but significant effect on T1 (12,14). VBM commonly relies on T1w imaging. Brain iron appears to lower signal-to-noise ratio (SNR ; signal intensity of GM), resulting in degraded T1 contrast (CNR) leading to GM volume assessment bias. (12,23)
Consequently, T1w-related VBM for analysis of subcortical structures is skewed and needs other MRI protocols to overcome iron-related bias.

Novel quantitative study methods in computational anatomy

During the last decade, quantitative MRI (qMRI), a whole-brain quantitative high-resolution imaging method has been developed with the purpose to allow microstructure tissue assessment. qMRI sequences are termed parameter maps. A parameter map provides a neuroimaging biomarker for brain compounds such as water, myelin or iron with absolute measures whereas weighted-imaging has arbitrary units. Those measures are thus comparable through time and between imaging centers. More recently, multiple parameter mapping (MPM) protocols permit generation of the different parameter maps in one acquisition in clinically feasible duration. Analysis of parameter maps with voxel-based quantification (VBQ) provides quantitative data enabling interindividual comparison or intraindividual comparison over time. Common parameter maps are longitudinal relaxometry rate R1 (1/T1) and effective transverse relaxation rate R2* (1/T2*), effective proton density PD* and magnetization transfer saturation MT (figure 3). R2* is a surrogate marker for iron, MT for myelin and PD* for water (24,25). Postmortem validation has shown high correspondence between R2* and iron content and between MT and myelin content (26–29).

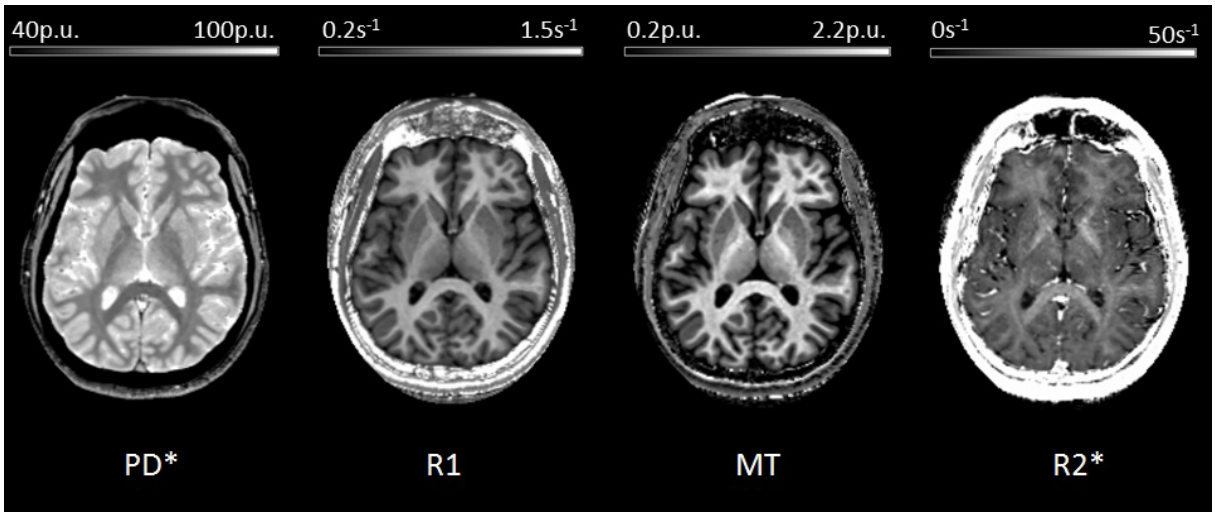

Figure 3 : Parameter maps of effective proton density PD*, longitudinal relaxometry rate R1, magnetization transfer saturation MT and effective transverse relaxation rate R2* (26)**.**

This quantitative approach has been introduced for basal ganglia by *Helms et al.* using parameter maps based on magnetization transfer (MT) imaging and has proved to provide excellent CNR and no contrast interference due to iron (12,30).
Magnetization transfer (MT) saturation imaging is a technique that relies on the transfer of energy from very mobile protons of free water to highly bound protons within macromolecules such as myelin. This energy transfer content is done by application of off-resonant radiofrequency (RF) pulses prior to excitation and leads to magnetization saturation of macromolecular protons. In voxels with a higher macromolecular content, the mobile water will experience a greater percentage loss of signal. Consequently, measures of MT provide information about the macromolecular content of the microstructural environment and reliable myelin surrogate marker (24,27,31,32).

Why are novel methods not extensively used in clinical practice ?
Automated segmentation relies on adequate and accurate TPMs (33). Currently, such TPMs are T1-based and do not provide sufficient accuracy for deep gray matter (34). Recent attempts to improve tissue priors according to new MRI protocols have been made but fail to offer adequate data due to low number of subjects, restraint age-span, gender restriction (35–37). Thus clinical application of state of the art MPM-derived morphometry for basal ganglia is not achievable in absence robust and accurate TPMs.

Aim

The aim of this work is to create an accurate TPM with new tissue priors for the basal ganglia and the main subcortical structures based on MT and R2* parameter maps to obtain the full range of useful microstructural information they provide, biomarkers for myelin and iron respectively, and optimal contrast for these nuclei without iron-related bias of usual MRI protocols. To build robust tissue priors, we used a manual delineation technique with different raters on a cohort of a large number of healthy subjects with comparable representation of gender and wide adult age-span. To provide extensive subcortical TPM, tissue priors included the CN, putamen, GP, thalamus, STN, SN, RN and the cerebellar dentate nucleus (DN).

To assess the results of our study, we evaluated manual delineation reliability between raters and tested accuracy of newly established TPM by comparing it to the used TPM to date. We further studied age-related microstructural changes with the aid of the new TPM.

Hypothesis

The new TPM will provide more anatomically plausible tissue classification of basal ganglia than the previous ones, especially in context of age-related microstructural changes involving increase of subcortical iron concentration.

Materials & Methods

Materials

Demographics

Human *in vivo* whole-brain images were obtain from a cohort of 96 healthy adults with 40 males with an age ranging from 27 to 74 years old (mean 55 ± 15) ; 56 females with an age from 21 to 88 years old, (mean 57 ± 19). All subjects gave written informed consent for use of their anonymized data in studies led by the responsible investigator. The local ethics committees approved all experimental protocols. Subjects with macroscopic abnormalities, cerebrovascular lesions, significant age-related WM hyperintensities (grade 2 or more on Scheltens' scale (38)) and major brain atrophy (measured with the brain volume fraction (39)) have been previously excluded from the cohort.

MRI protocol

We performed qMRI with a 3T scanner, in order to get for each subject, MT, R1 and R2* maps with 1 mm^3 isotropic resolution, corrected for B0 and B1 inhomogeneities. The total acquisition time was 24 minutes.

To test our new TPM on T1w images, we used a second set of images, previously used in the study of *Helms et al, 2009* (12). The dataset used Modified Driven Equilibrium Fourier Transform (MDEFT), an optimized T1w MRI protocol for VBM, on a cohort of 20 women with an age range 22-85 years old (mean age 37 ±13) and 13 men with an age range 18-73 years old (mean age 47 ±19). The images have 1 mm^3 isotropic resolution and an acquisition time 13 minutes.

Methods

Manual delineation on atlas-based labeling

Manual delineation was performed on an online web browser-based tool that displayed the subjects' images in native space with MT and R2* parameter maps and the three anatomical planes. Binary segmentation masks for the CN, putamen, GP, thalamus, STN, SN, RN and DN have been retrieved from reference atlases (40–44) and warped from normalized space to each subject's native space. Four raters, consisting of master medical student and PhD students in neuroscience, adjusted manually each mask to the subject's anatomy using either parameter map that offered best anatomical visualization. Refined masks were assessed by a neuroimaging specialized neurologist (B.D.) and neurosciences doctoral student with extensive brain anatomy expertise (S.L.).

Evaluation of manual delineation reliability between raters was performed using two statistical coefficients : Dice index and Cohen's kappa coefficient. Dice index is a similarity coefficient that provides the ratio of agreement between two samples (45). Cohen's kappa coefficient is an inter-rater agreement coefficient and provides more robust measure than simple percent agreement calculation, since it takes into account the agreement occurring by chance (46).

Creation of TPM

Manually adjusted masks by raters were registered in normalized MNI space. Then the normalized masks from the different raters for each structure were averaged and smoothened to obtain probability maps for their corresponding structure. Those probability maps were registered into SPM12, unified and combined with conventional TPM to provide the new whole-brain TPM with updated tissue priors (GM, WM, CSF and "other") for the subcortical structures.

Assessment and validation of new TPM

Validation of new TPM

To assess the anatomical reliability of the new TPM in comparison of the old one we used two statistical analyses. The first one compares GM volumes of each structure on MT maps using the new and old TPM. The second one compares agreement of manual segmentation of each structure with the applied new and old TPM.

The GM volume comparison was carried out with a leave-one-out cross validation. For this statistical analysis, the new TPM was elaborated with the results of manual delineation except for one that was not included. Both the resulting new TPM and old TPM were then applied to the excluded MT map for tissue classification in SPM12. GM volumes were next calculated with a minimal 0,2 GM probability threshold for every voxel that have been previously selected by all raters. This process has been repeated excluding all the different MT maps. GM volume for each structure is given with the mean of all the obtained GM volumes. The GM volume comparison between the new and old TPM was realized using a paired t-test in SPSS22.

The agreement assessment between manual delineation and both TPMs has been realized using the Dice index. Once again, only the voxels labeled by all raters in manual delineation for each structure have been taken into account. Voxels for the old and new TPM have been selected using two different minimal GM probability thresholds of 0,2 and 0,5 in each structure in SPM12. Dice indexes have been calculated for both thresholds, for both TPMs, in relation to the manual delineation. Next we used a paired t-test to compare the mean of Dice indexes for each structure in SPSS22.

We further identified structures that had volume loss as a result of misclassification, due to age-related loss of contrast, by the old TPM rather than mere overall age-independent decreased CNR between MT and T1w maps. We compared the Dice index differences, between the old and new TPM and for each structure, and age using paired t-tests. We retained only the t-values with a $p<0,05$ statistical significance level.

Validation of robustness of new TPM in age-related microstructural changes

To assess robustness of the new TPM against age-related loss of contrast caused by iron concentration increase, we used two voxel-based regressions with SPM12 in the structures where paired t-tests have shown significant differential age-related volume loss between old and new TPM on MT images. First, we performed a linear regression analysis between GM volume loss and R2* parameter map to identify misclassified areas due to iron concentration increase. T-values of voxel-based regressors have been determined to provide visual scaling.

Then, a regression analysis between age and R2* map was carried out to distinguish areas amongst the basal ganglia that are subject to iron concentration increase with age. T-values of voxels with positive correlation were also displayed on a visual scale.

Results

Inter-rater reliability

The mean Dice index range was between 0.65 and 0.87 and the mean Cohen's kappa coefficient between 0.70 and 0.87. Overall, it is an excellent inter-rater agreement. The structures providing the best agreement were the CN, putamen, GB and thalamus with Cohen's kappa coefficients mainly above 0.8. The SN, RN, STN showed smaller agreement and dentate with coefficients below 0.8 and with the highest percentages of disagreement (table 1).

Structure		Volume (mm^3)		% of disagreement voxel		Dice index		Cohen's kappa	
		Mean	SD	Mean	SD	Mean	SD	Mean	SD
Caudate	Left	3421	900	17	3	0.83	0.06	0.85	0.06
	Right	3306	700	16	3	0.85	0.06	0.86	0.06
Putamen	Left	3906	650	19	3	0.80	0.05	0.8	0.05
	Right	3966	690	18	4	0.85	0.03	0.86	0.03
GP	Left	1319	235	20	4	0.79	0.08	0.8	0.08
	Right	1263	201	21	5	0.76	0.09	0.77	0.09
Thalamus	Left	5110	1100	16	4	0.86	0.04	0.86	0.04
	Right	5495	1301	15	3	0.87	0.05	0.87	0.05
SN	Left	330	94	25	6	0.70	0.11	0.74	0.12
	Right	330	90	23	5	0.76	0.14	0.77	0.14
RN	Left	220	49	29	7	0.68	0.13	0.71	0.13
	Right	220	50	28	8	0.69	0.11	0.77	0.11
STN	Left	86	28	33	7	0.65	0.14	0.70	0.12
	Right	85	20	31	7	0.70	0.1	0.73	0.19
Dentate	Left	1032	215	20	5	0.76	0.11	0.73	0.11
	Right	1013	195	23	6	0.77	0.14	0.76	0.13

Table 1 : Inter-rater reliability. Mean volumes delineated by raters, percentage of disagreement between raters and agreement coefficients.

Validation of new TPM

Application of the new TPM on MT images showed significantly greater volumes in all structures, all above critical t-values (1,98 ; $p < 0.05$). The GP, thalamus, SN, RN, STN and DN showed the biggest volume improvements with t-values mainly above 10. The CN and putamen had lower volume improvements (table 2).

The new TPM was associated with significantly better agreement than the old TPM with manual delineation for all structures and both 0.2 and 0.5 GM probability threshold (table 2).

Structures associated with significant volume loss as a result of misclassification by the old TPM due to age-related contrast bias are the CN, putamen and RN (table 2).

Structure		Volume in mm^3 new TPM (Mean±SD)	Volume in mm^3 old TPM (Mean±SD)	T-value $Vol_{newTPM} > Vol_{oldTPM}$	T-value $DI_{newTPM} > DI_{oldTPM}$ Th 0.2	T-value $DI_{newTPM} > DI_{oldTPM}$ Th 0.5	T-value ΔDI vs age Th 0.2	T-value ΔDI vs age Th 0.5
Caudate	Left	3482±310	3181±396	4	10.8	13.0	6.8	4.1
	Right	3420±305	2838±399	5	10.4	4.9	7	4.37
Putamen	Left	3372±401	2879±470	4.8	14.1	10.0	5	5.4
	Right	3598±401	2870±470	4.3	14.5	9.4	6	5.82
GP	Left	1032±203	402±112	17.8	36.4	32.6	-	-
	Right	1195±211	373±130	18.2	45.4	35.7	-	-
Thalamus	Left	4876±705	3160±473	14.1	51.8	49	-	-
	Right	5077±837	3791±547	14.3	39.8	48.7	-	-
SN	Left	293±52	226±45	10	38.4	38.4	-	-
	Right	316±66	242±61	9.5	32.9	32.3	-	-
RN	Left	50±10	7±4	12.7	14.8	10.2	11.1	5
	Right	52±10	6±4	13.8	14.3	10.2	11.7	5.3
STN	Left	32±7	9±6	8.5	10.7	9.6	-	-
	Right	33±8	9±4	10.7	12.3	10.6	-	-
Dentate	Left	977±140	122±60	16.8	26.5	21.8	-	-
	Right	987±125	106±50	15.5	20.5	14	-	-

Table 2 : Validation of new TPM. Comparison of GM volumes between old and new TPM *(columns 1,2,3)*. Comparison of agreement between old and new TPMs with manual segmentation *(columns 4,5)*. Structures with higher age-related GM volume loss with old TPM *(columns 6,7).*

Validation of robustness of the new TPM

We found a positive linear correlation of GM volume loss associated with age-related microstructural changes resulting in classification bias only in the dorso-lateral putamen with the old TPM compared to the new TPM.

A positive correlation was also found between R2* and age in the entire putamen, CN, ventral GP, confirming iron concentration increase with age in those structures. R2* parameter map is also confirmed to suit iron-rich structure detection for the creation of the new TPM.

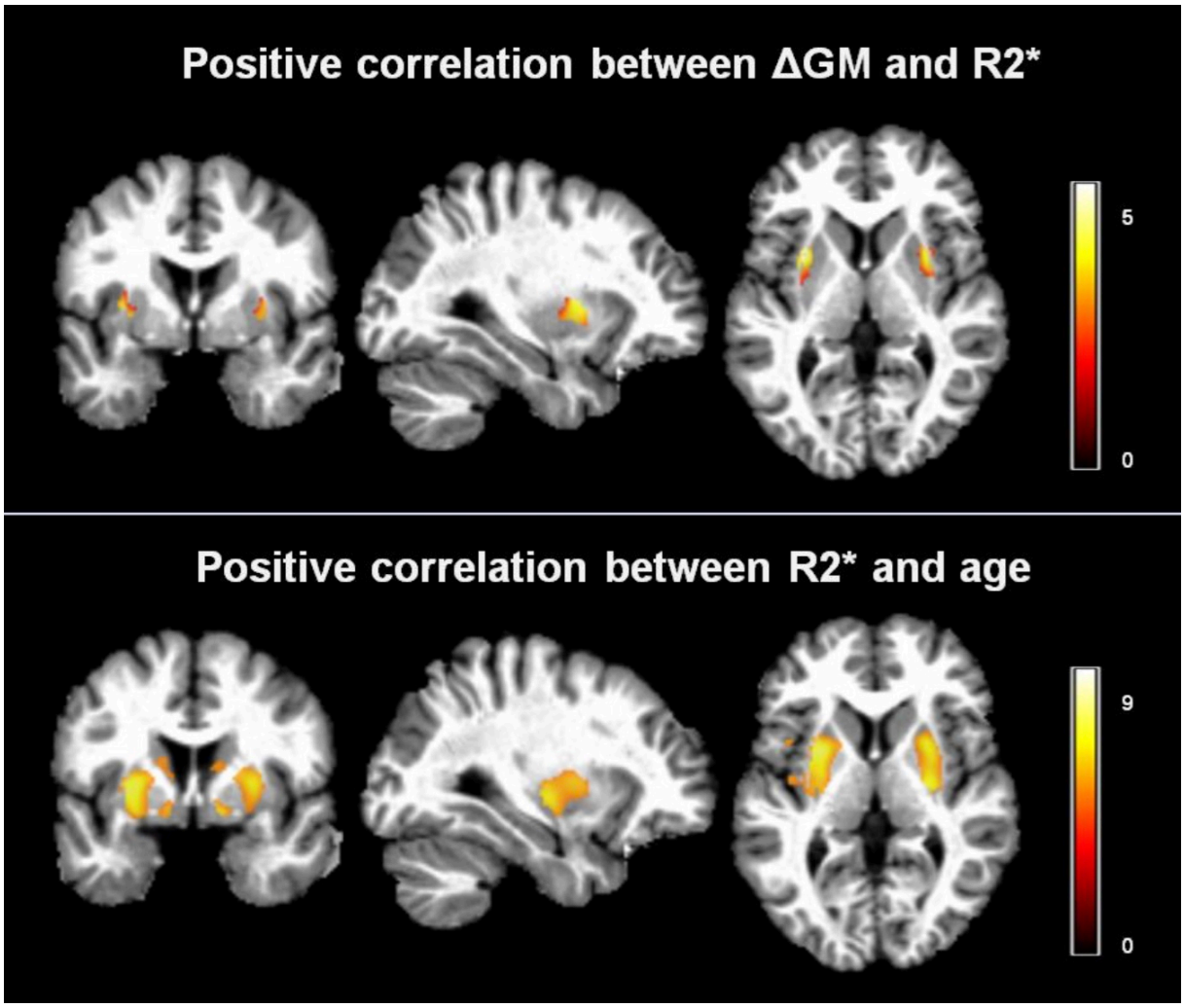

Figure 4 : Top figure : voxel t-values with positive correlation between R2* (iron biomarker) and higher age-related GM volume loss with conventional TPM. **Bottom figure** : voxel t-values with positive correlation between R2* and age.

Discussion and conclusion

We created new tissue priors for the subcortical structures based on magnetization transfer saturation (MT) and effective transverse relaxation rate (R2*) parameter maps proved to be more accurate than currently used T1w-based tissue probability maps (TPMs). The new TPM was built from a manual delineation technique using different raters on a cohort with a large number of subjects with comparable representation gender and with a wide adult age range. To date, no other study provided tissue priors based on a large and representative sample of the whole adult population using new quantitative approaches.

The inter-rater agreement and reliability of the manual delineation results were excellent in regard of other studies (13,35,37). Structures such as the subthalamic nucleus, substantia nigra, red nucleus and cerebellar dentate nucleus had lower inter-rater agreement, probably due to their smaller size, lower contrast than the basal ganglia and partial volume effect limiting segmentation accuracy.

The application of the new TPM on MT parameter maps demonstrated higher accuracy than the old TPM with a significant improvement of volume detection amongst all subcortical structures. Therefore, automated tissue classification has been optimized.

Iron deposits in subcortical structures has been shown to be associated with poorer contrast-to-noise ratio in weighted MR imaging (11–13). Postmortem biochemical analysis have shown iron concentration increase with age, degrading GM signal resulting in further misclassification (19,22). Parameter maps used in quantitative MRI have shown to be a valuable asset to overcome contrast bias and provide surrogate biomarkers with absolute measures for various compounds of the brain, including water, myelin and iron (12,24,25). By using R2* parameter map, we were able not only to obtain better segmentation using the iron marker in iron-rich nuclei such as the substantia nigra, red nucleus and subthalamic nucleus to elaborate the new TPM, but also quantify GM volume loss due to iron contrast bias in the old TPM and demonstrate specific areas in basal ganglia associated with increased iron deposition in the aging adult – namely the entire putamen, the ventral globus pallidus and caudate nucleus. Those results demonstrated increased robustness of the new TPM against high iron-related contrast degradation in the elderly subject. The TPM robustness is explained by the use of parameter maps in the creation of the tissue priors and inclusion of old subjects.

In conclusion, the new TPM is suitable to improve VBM of the basal ganglia and the other subcortical nuclei, and opens up to the clinical use of new quantitative approaches for the volumetric assessment of the brain.

Acknowledgments

I would like to thank my fellow master students that contributed to this work : Gaëlle Waetherill, Céline Gilioz et Yanick Derighetti.
Warmest thanks to Martina Callaghan, from Wellcome Trust Centre for Neuroimaging at University College London, and the Huntington's Disease Outreach Project for Education at Stanford (HOPES) for giving me the permission to use their illustrations.
Finally, special thanks to my tutor, Professor Bogdan Draganski, and co-tutor, Sara Lorio, for guidance and advices through the different aspects and the long process this work has been.

References

1. Haber SN. The place of dopamine in the cortico-basal ganglia circuit. Neuroscience. 2014 Dec;282:248–57.

2. Draganski B, Kherif F, Kloppel S, Cook PA, Alexander DC, Parker GJM, et al. Evidence for Segregated and Integrative Connectivity Patterns in the Human Basal Ganglia. J Neurosci. 2008 Jul 9;28(28):7143–52.

3. Utter AA, Basso MA. The basal ganglia: An overview of circuits and function. Neurosci Biobehav Rev. 2008 Jan;32(3):333–42.

4. McGuire P, Bench C, Frith C, Marks I, Frackowiak RS, Dolan R. Functional Anatomy of Obsessive-Compulsive Phenomena. Br J Psychiatry. 1994;164(4):459–68.

5. Meunier S, LehÉricy S, Garnero L, Vidailhet M. Dystonia: Lessons from Brain Mapping. The Neuroscientist. 2003 Feb 1;9(1):76–81.

6. DeLong MR, Wichmann T. Basal Ganglia Circuits as Targets for Neuromodulation in Parkinson Disease. JAMA Neurol. 2015 Nov 1;72(11):1354.

7. Herrington TM, Cheng JJ, Eskandar EN. Mechanisms of deep brain stimulation. J Neurophysiol. 2015 Oct 28;jn.00281.2015.

8. Tekriwal A, Baltuch G. Deep Brain Stimulation: Expanding Applications. Neurol Med Chir (Tokyo) [Internet]. 2015 [cited 2015 Dec 2]; Available from: https://www.jstage.jst.go.jp/article/nmc/advpub/0/advpub_ra.2015-0172/_article

9. May A, Gaser C. Magnetic resonance-based morphometry: a window into structural plasticity of the brain. Curr Opin Neurol. 2006;19(4):407–11.

10. Ashburner J, Friston KJ. Unified segmentation. NeuroImage. 2005 Jul;26(3):839–51. Figure used with permission of publisher.

11. Wonderlick J, Ziegler D, Hosseinivarnamkhasti P, Locascio J, Bakkour A, Vanderkouwe A, et al. Reliability of MRI-derived cortical and subcortical morphometric measures: Effects of pulse sequence, voxel geometry, and parallel imaging. NeuroImage. 2009 Feb 15;44(4):1324–33.

12. Helms G, Draganski B, Frackowiak R, Ashburner J, Weiskopf N. Improved segmentation of deep brain grey matter structures using magnetization transfer (MT) parameter maps. NeuroImage. 2009 Aug;47(1):194–8.

13. Babalola KO, Patenaude B, Aljabar P, Schnabel J, Kennedy D, Crum W, et al. An evaluation of four automatic methods of segmenting the subcortical structures in the brain. NeuroImage. 2009 Oct;47(4):1435–47.

14. Schenck JF. Magnetic resonance imaging of brain iron. J Neurol Sci. 2003;207(1):99–102.

15. Schenck JF, Zimmerman EA. High-field magnetic resonance imaging of brain iron: birth of a biomarker? NMR Biomed. 2004 Nov;17(7):433–45.

16. Shmueli K, de Zwart JA, van Gelderen P, Li T-Q, Dodd SJ, Duyn JH. Magnetic susceptibility mapping of brain tissue in vivo using MRI phase data. Magn Reson Med. 2009 Dec;62(6):1510–22.

17. Berg D, Youdim MB. Role of iron in neurodegenerative disorders. Top Magn Reson Imaging. 2006;17(1):5–17.

18. Connor J, Snyder B, Beard J. Regional distribution of iron and iron-regulatory proteins in the brain in aging and disease. J Neurosci Res. 1992;31(2):327–35.

19. Gelman B. Iron in CNS disease. J Neuropathol Exp Neurol. 1995;54(4):477–86.

20. Haacke EM, Cheng NYC, House MJ, Liu Q, Neelavalli J, Ogg RJ, et al. Imaging iron stores in the brain using magnetic resonance imaging. Magn Reson Imaging. 2005 Jan;23(1):1–25.

21. Connor J, Menzies S, St Martin S. Cellular distribution of transferrin, ferritin, and iron in normal and aged human brains. J Neurosci Res. 1990;27(4):595–611.

22. Haacke EM, Miao Y, Liu M, Habib CA, Katkuri Y, Liu T, et al. Correlation of putative iron content as represented by changes in R2* and phase with age in deep gray matter of healthy adults. J Magn Reson Imaging. 2010 Aug 27;32(3):561–76.

23. Lorio S, Lutti A, Kherif F, Ruef A, Dukart J, Chowdhury R, et al. Disentangling in vivo the effects of iron content and atrophy on the ageing human brain. NeuroImage. 2014 Dec;103:280–9.

24. Draganski B, Ashburner J, Hutton C, Kherif F, Frackowiak RSJ, Helms G, et al. Regional specificity of MRI contrast parameter changes in normal ageing revealed by voxel-based quantification (VBQ). NeuroImage. 2011 Apr;55(4):1423–34.

25. Weiskopf N, Suckling J, Williams G, Correia MM, Inkster B, Tait R, et al. Quantitative multi-parameter mapping of R1, PD*, MT, and R2* at 3T: a multi-center validation. Front Neurosci. 2013;7.

26. Callaghan MF. Quantitative MRI and Voxel-Based Quantification (VBQ) [Internet]. Wellcome Trust Centre for Neuroimaging, UCL; Available from: http://www.fil.ion.ucl.ac.uk/Research/physics_info/QuantMRI_VBM.html. Figure used with permission of author.

27. Callaghan MF, Helms G, Lutti A, Mohammadi S, Weiskopf N. A general linear relaxometry model of R_1 using imaging data: General Linear Relaxometry Model of R1. Magn Reson Med. 2015 Mar;73(3):1309–14.

28. Schmierer K, Scaravilli F, Altmann DR, Barker GJ, Miller DH. Magnetization transfer ratio and myelin in postmortem multiple sclerosis brain. Ann Neurol. 2004 Sep;56(3):407–15.

29. Langkammer C, Schweser F, Krebs N, Deistung A, Goessler W, Scheurer E, et al. Quantitative susceptibility mapping (QSM) as a means to measure brain iron? A post mortem validation study. NeuroImage. 2012 Sep;62(3):1593–9.

30. Helms G, Dathe H, Kallenberg K, Dechent P. High-resolution maps of magnetization transfer with inherent correction for RF inhomogeneity and T1 relaxation obtained from 3D FLASH MRI. Magn Reson Med. 2008;60(6):1396–407.

31. Lehéricy S, Sharman MA, Santos CLD, Paquin R, Gallea C. Magnetic resonance imaging of the substantia nigra in Parkinson's disease. Mov Disord. 2012 Jun;27(7):822–30.

32. Helms G, Dathe H, Kallenberg K, Dechent P. High-resolution maps of magnetization transfer with inherent correction for RF inhomogeneity and T_1 relaxation obtained from 3D FLASH MRI. Magn Reson Med. 2008 Dec;60(6):1396–407.

33. Ahsan RL, Allom R, Gousias IS, Habib H, Turkheimer FE, Free S, et al. Volumes, spatial extents and a probabilistic atlas of the human basal ganglia and thalamus. NeuroImage. 2007 Nov 1;38(2):261–70.

34. Mazziotta J, Toga A, Evans A. A probabilistic atlas and reference system for the human brain: International Consortium for Brain Mapping (ICBM). Philos Trans R Soc Lond B Biol Sci. 2001;29(356):1293–322.

35. Ahsan RL, Allom R, Gousias IS, Habib H, Turkheimer FE, Free S, et al. Volumes, spatial extents and a probabilistic atlas of the human basal ganglia and thalamus. NeuroImage. 2007 Nov 1;38(2):261–70.

36. Lim IAL, Faria AV, Li X, Hsu JTC, Airan RD, Mori S, et al. Human brain atlas for automated region of interest selection in quantitative susceptibility mapping: Application to determine iron content in deep gray matter structures. NeuroImage. 2013 Nov;82:449–69.

37. Keuken MC, Bazin P-L, Crown L, Hootsmans J, Laufer A, Müller-Axt C, et al. Quantifying inter-individual anatomical variability in the subcortex using 7T structural MRI. NeuroImage. 2014 Jul;94:40–6.

38. Scheltens P, Barkhof F, Leys D, Pruvo JP, Nauta JJ, Vermersch P, et al. A semiquantative rating scale for the assessment of signal hyperintensities on magnetic resonance imaging. J Neurol Sci. 1993;114:7–12.

39. Rudick RA, Fisher E, Lee J-C, Simon J, Jacobs L, others. Use of the brain parenchymal fraction to measure whole brain atrophy in relapsing-remitting MS. Neurology. 1999;53(8):1698–1698.

40. Diedrichsen J. A spatially unbiased atlas template of the human cerebellum. NeuroImage. 2006 Oct;33(1):127–38.

41. Lancaster JL, Woldorff MG, Parsons LM, Liotti M, Freitas CS, Rainey L, et al. Automated Talairach atlas labels for functional brain mapping. Hum Brain Mapp. 2000;10(3):120–31.

42. Goldstein JM, Seidman LJ, Makris N, Ahern T, O'Brien LM, Caviness VS, et al. Hypothalamic Abnormalities in Schizophrenia: Sex Effects and Genetic Vulnerability. Biol Psychiatry. 2007 Apr;61(8):935–45.

43. Morel A, Magnin M, Jeanmonod D. Multiarchitectonic and Stereotactic Atlas of the Human Thalamus. J Comp Neurol. 1997;387:588–630.

44. Prodoehl J, Yu H, Little DM, Abraham I, Vaillancourt DE. Region of interest template for the human basal ganglia: Comparing EPI and standardized space approaches. NeuroImage. 2008 Feb;39(3):956–65.

45. Dice LR. Measures of the Amount of Ecologic Association Between Species. Ecology. 1945;26:297–302.

46. Cohen J. A Coefficient of Agreement for Nominal Scales. Educ Psychol Meas. 1960;20:37–46.